



# Calculations of the integrated cross sections in dressed carbon-ion collisions with atomic hydrogen

N. W. Antonio <sup>1,\*</sup>, C. T. Plowman,<sup>1</sup> I. B. Abdurakhmanov,<sup>2</sup> and A. S. Kadyrov <sup>1,3</sup>

<sup>1</sup>*Department of Physics and Astronomy, Curtin University, GPO Box U1987, Perth, Western Australia 6845, Australia*

<sup>2</sup>*Pawsey Supercomputing Research Centre, 1 Bryce Avenue, Kensington, Western Australia 6151, Australia*

<sup>3</sup>*Institute of Nuclear Physics, Ulugbek, 100214 Tashkent, Uzbekistan*



(Received 10 November 2023; accepted 5 January 2024; published 26 January 2024)

The two-center wave-packet convergent close-coupling approach is extended to model dressed ion collisions with atomic hydrogen. This is done by reducing the problem to an effective three-body one and using a model potential to approximate the interactions between the projectile ion with the target electron and target nucleus. The method is applied to calculate the total ionization cross section along with the total and  $n$ -resolved electron-capture and target-excitation cross sections in partially stripped  $C^{2+}$  and  $C^{3+}$  ion collisions with ground-state atomic hydrogen. Calculations are performed across a broad projectile energy range from 1 keV/u to 1 MeV/u, where one-electron collision processes are dominant. The calculated total electron-capture cross sections for both systems generally agree very well with available experimental and previous theoretical data. We find that at incident energies above 100 keV/u the total electron-capture cross sections in dressed carbon-ion collisions are larger than the ones corresponding to collisions of bare projectile ions of the same charge. A possible reason for this could be associated with the target-electron radial density and the behavior of the potential of interaction between the target electron and the carbon ion. Our results for ionization in  $C^{3+} + H(1s)$  collisions overestimate the experimental data. We also report a set of calculations for ionization in  $C^{2+} + H(1s)$  collisions.

DOI: [10.1103/PhysRevA.109.012817](https://doi.org/10.1103/PhysRevA.109.012817)

## I. INTRODUCTION

Collisions between partially stripped ions and atoms are important from a fundamental point of view. Given the multi-electron nature of these systems, they allow us to explore the role electron-electron interactions play in the overall collision dynamics. Furthermore, there are many practical applications that would benefit from a complete understanding of these collisions. Modeling x-ray spectra from comets [1,2] and hadron therapy for cancer treatment [3,4] are just two examples of areas that require accurate data from these collisions. The development of hadron therapy as a method for treating cancer has raised the importance of studying dressed carbon-ion collisions in particular [5]. This modern cancer treatment technique uses beams of protons and heavier ions such as  $C^{6+}$  ions to bombard tumor sites and destroy cancerous tissue. The advantage of this treatment over x-ray therapy is that it significantly minimizes the damage to the surrounding healthy tissues. This is possible because heavy ions deposit most of their energy in the region of the Bragg peak towards the end of the beam path. To ensure the Bragg peak occurs at the location of a tumor site, extensive treatment planning is required. This includes depth-dose simulations which rely on accurate stopping power cross sections for collisions involving the beam ions and biological molecules. As the initially bare ions travel through the medium, they can capture one or more electrons forming partially stripped ions [4,6]. Therefore, modeling partially stripped ion collisions is very important for radiation dose simulations. Calculating stopping

power cross sections for bare and dressed carbon-ion collisions with the water molecule  $H_2O$  is of great importance for radiation-dose simulations [7]. However, to begin developing a theory capable of accurately modeling such systems, studying these collisions with prototypal targets such as atomic and molecular hydrogen is an important first step.

Obtaining accurate total and partial cross sections for electron capture (EC), target excitation, and ionization in dressed ion collisions with atomic hydrogen is also necessary to perform impurity diagnostics in fusion plasmas [8]. In particular, major fusion projects such as the International Thermonuclear Experimental Reactor and the Joint European Torus are expected to contain dressed impurity species such as carbon, oxygen, nitrogen, beryllium, and tungsten ions. These impurities form through either ion seeding [9] or by erosion of plasma facing components [10]. How these impurity ions affect properties of the plasma such as its temperature and density can be investigated using the charge-exchange recombination spectroscopy (CXRS) technique [11]. A beam of neutral hydrogen will be injected into the reactor so that collisions between impurity ions and atomic hydrogen can occur. These events may lead to charge-exchange processes whereby dressed ions of various charge states form in excited states. The CXRS approach to performing diagnostics on fusion plasmas is to analyze the spectra of these ions as they emit photons, through de-excitation processes, to determine ion densities. This requires accurate cross-section data for all possible collision processes including electron capture, ionization, and target excitation [12].

There are a number of experimental studies on partially stripped carbon-ion collisions with atomic hydrogen across a broad range of projectile energies. In particular, the total

\*nicholas.antonio@postgrad.curtin.edu.au

and partial electron-capture cross sections for  $C^{2+}$  and  $C^{3+}$  collisions with H in the ground state were measured by McCullough *et al.* [13], at energies from 50 eV/u to 1.5 keV/u. Further measurements of the partial EC cross sections at low energies in  $C^{3+} + H(1s)$  collisions by Wilkie *et al.* [14] and Ćirić *et al.* [15] found good agreement with prior results by McCullough *et al.* [13]. For  $C^{2+} + H(1s)$  collisions, the total electron-capture cross section was measured across an energy range from 40 eV/u to 200 keV/u by Nutt *et al.* [16], Phaneuf *et al.* [17], Goffe *et al.* [18], and Gardner *et al.* [19]. References [17] and [18] also obtained data for the total EC cross section at intermediate energies in  $C^{3+} + H(1s)$  collisions. Overall, there is good agreement between the two sets of measurements, except around 10 keV/u, where results differ by approximately 34%. At low energies, the total EC cross section for  $C^{2+}$  collisions was measured by Phaneuf *et al.* [20] and Havener *et al.* [21]. Measurements for the total ionization cross section in both  $C^{2+}$  and  $C^{3+}$  collisions with H were reported by Shah and Gilbody in Refs. [22,23]. Overall, this collection of experimental data involving dressed carbon-ion collisions with atomic hydrogen provides a solid foundation to test theories of such collisions.

There are a number of distinct theoretical methods developed to study ion-atom collisions [24]. The molecular-orbital close-coupling (MOCC) approach [25,26] is applicable at low projectile energies, whereas in the intermediate- to high-projectile-energy domains the first-order perturbation approach with corrected boundary conditions [27], the classical trajectory Monte Carlo (CTMC) method [28,29], the two-center basis-generator method (TC-BGM) [30], the semi-classical two-center atomic-orbital close-coupling (AOCC) [31–33] approach, and lattice-based approaches [34,35] can be used.

Modeling dressed ion-atom collisions in a completely *ab initio* manner is challenging due to the multielectron structure inherent to these systems. It has been shown that even developing a theory for collisions involving two-electron targets requires some approximations (see, for example, Refs. [36,37]). An alternative approach to study single-electron processes taking place in dressed ion collisions is to employ an effective potential that treats the interactions with the multielectron ion in a spherically symmetric manner [38]. This allows one to represent the scattering system as an effective three-body problem with a single active electron. The accuracy of such an approach depends on a number of factors including the projectile energy range, the charge of the ion, and the model potential used to describe the multielectron projectile.

Many theoretical approaches to ion-atom collisions were applied to study dressed carbon-ion collisions. Errea *et al.* [39] studied EC processes in  $C^{2+} + H(1s)$  collisions using the MOCC method at incident energies between 8 eV/u and 25 keV/u. In earlier experiments [13] it was unclear what effect an unknown percentage of metastable  $^3P$   $C^{2+}$  projectiles had on the measurements of the EC cross section. Errea *et al.* found no strong evidence of metastable contamination of the beam. They showed that any possible effect due to the contribution of the metastable  $^3P$  projectile ion beam would only be important at energies below 0.1 keV/u. Using the electron-nuclear dynamics (END) method, Guevara *et al.* [40]

calculated the total EC cross sections in  $C^{3+} + H(1s)$  collisions from 0.1 eV/u to 10 keV/u. At higher energies, between 10 and 200 keV/u, there are a number of theoretical calculations for the total and state-selective EC cross sections of dressed carbon-ion collisions with H which use the CTMC [41–44], AOCC [45], boundary-corrected initial state (BCIS) [46], END [40], and two-center basis-generator [30] methods. However, the only calculation for the total ionization cross section in  $C^{3+} + H(1s)$  collisions available is by Leung and Kirchner [30]. There has been no previous theoretical investigation of the ionization process in  $C^{2+} + H(1s)$  collisions.

In this work we incorporate an effective potential into the two-center wave-packet convergent close-coupling (WP-CCC) approach to three-body problems [47,48] to study dressed carbon-ion collisions with atomic hydrogen. In this approach we expand the total scattering wave function in terms of bound and pseudocontinuum states around both centers to account for transitions to all final channels. The WP-CCC method has been applied to study a variety of multiply charged bare-ion collisions with atomic hydrogen such as  $He^{2+}$  [49],  $Li^{3+}$  [50],  $Be^{4+}$  [51–53],  $C^{6+}$  [48], and  $Ne^{10+}$  [54] collisions with H. The obtained results compare favorably with available experimental data, which demonstrates the method's utility in studying three-body ion-atom collisions. In this paper, as a proof of principle, we test this model potential WP-CCC approach to dressed ion collisions by first applying it to  $C^{2+}$  and  $C^{3+}$  ion collisions with  $H(1s)$ . These two carbon ions were chosen as they have a sufficient number of bound electrons to highlight differences in the cross sections when comparing them to results for collisions with the corresponding bare projectile ions with the same charge. The total and  $n$ -resolved cross sections are presented for electron capture, target excitation, and ionization in these two collision systems. These calculations are performed at collision energies ranging from 1 keV/u to 1 MeV/u, where coupling between the channels is important. We compare the results with experimental measurements and previous theoretical calculations where available.

The remainder of this paper is structured as follows. We begin by giving an overview of the WP-CCC formalism in Sec. II, where we highlight changes to the method needed to study dressed ion collisions with H. In Sec. III the details of the calculations are given. The results of the calculations are presented in Sec. IV. In Sec. V we summarize and draw conclusions from this study. Unless specified otherwise, atomic units are used throughout this paper.

## II. TWO-CENTER WAVE-PACKET CONVERGENT CLOSE-COUPPLING FORMALISM

The formalism of the WP-CCC approach to bare-ion collisions with atomic hydrogen is given in Refs. [47,48]. In this paper we extend the approach to model partially stripped ion collisions with atomic hydrogen. This is done by treating the problem as an effective three-body one. The formalism is similar to the bare ion-hydrogen case; however, the form of the interaction between the projectile ion with the active electron and target nucleus will be different. Hence, in this section we will primarily cover aspects of theory that require changing when the functional form of the scattering potential changes.

### A. Close-coupling equations

Let us consider a dressed ion scattering from the hydrogen atom. We call the electron that is initially bound to the target proton the active electron. We refer to the projectile nucleus and its bound electrons collectively as the projectile ion. This way we describe the scattering problem as an effective three-body one. The system is described using Jacobi coordinates. Vectors  $\mathbf{r}_T$  and  $\mathbf{r}_P$  denote the position of the active electron relative to the target proton and projectile ion, respectively. The position of the projectile ion relative to the center of mass of the target is given by  $\boldsymbol{\sigma}_T$ , while the position of the projectile-active electron pair relative to the target nucleus is  $\boldsymbol{\sigma}_P$ . The vector  $\mathbf{R}$  is the position of the projectile ion relative to the target center.

The effective three-body scattering wave function  $\Psi_i^+$ , subject to the outgoing-wave boundary conditions, is governed by the nonrelativistic time-independent Schrödinger equation (TISE)

$$(H - E)\Psi_i^+ = 0, \quad (1)$$

where  $H$  denotes the total Hamiltonian and  $E$  denotes the total energy of the collisional system. The index  $i$  specifies the initial channel. The Hamiltonian for the system consisting of the projectile ion, target proton, and active electron is written in the two equivalent forms

$$H = -\frac{1}{2\mu_T}\nabla_{\boldsymbol{\sigma}_T}^2 + H_T + \bar{V}_T \quad (2)$$

$$= -\frac{1}{2\mu_P}\nabla_{\boldsymbol{\sigma}_P}^2 + H_P + \bar{V}_P. \quad (3)$$

Here  $\mu_T$  is the reduced mass of the system in the channels where the electron is associated with the target and  $\mu_P$  is the reduced mass in the channels where the electron is associated with the projectile. The operators  $H_T$  and  $H_P$  are the target proton-electron and projectile ion-electron Hamiltonians, respectively. The potentials  $\bar{V}_T$  and  $\bar{V}_P$  are given as

$$\bar{V}_T = V_{\text{mod}}(R) - V_{\text{mod}}(r_P), \quad (4)$$

$$\bar{V}_P = V_{\text{mod}}(R) - \frac{1}{r_T}, \quad (5)$$

where  $V_{\text{mod}}$  is a model potential that represents the interactions the projectile ion experiences with the active electron and target proton. We use a model potential of the form

$$V_{\text{mod}}(r) = \frac{q_P}{r} + \frac{e^{-\zeta r}}{r} [(Z_P - q_P) + kr]. \quad (6)$$

Here  $q_P$  is the asymptotic charge of the projectile ion and  $Z_P$  is the projectile nucleus charge. The quantities  $\zeta$  and  $k$  are free parameters. Their values are determined in such a way that solving the effective one-electron (E1E) radial Schrödinger equation

$$\left( -\frac{1}{2} \frac{d^2}{dr^2} - \frac{1}{r} \frac{d}{dr} - \frac{q_P}{r} - \frac{e^{-\zeta r}}{r} [(Z_P - q_P) + kr] + \frac{\ell(\ell+1)}{2r^2} - \varepsilon_{n\ell} \right) R_{n\ell}(r) = 0 \quad (7)$$

for the radial wave function  $R_{n\ell}$  describing the projectile ion-electron system reproduces the ground-state orbital energy  $\varepsilon_{n\ell}$  given by the Hartree-Fock theory. The values of  $\zeta$  and  $k$  we use in this work to construct  $V_{\text{mod}}$  for the  $\text{C}^{2+}$  and  $\text{C}^{3+}$  projectiles are those presented in Ref. [46]. These were obtained with a variational method using the Hartree-Fock calculations performed by Clementi and Roetti [55].

To solve the effective three-body TISE (1), we expand the total scattering wave function using a basis consisting of  $N$  target-centered ( $\psi_\alpha$ ) and  $M$  projectile-centered ( $\psi_\beta$ ) pseudostates as

$$\Psi_i^+ \approx \sum_{\alpha=1}^N \tilde{F}_\alpha(\boldsymbol{\sigma}_T) \psi_\alpha(\mathbf{r}_T) e^{i\mathbf{k}_\alpha \cdot \boldsymbol{\sigma}_T} + \sum_{\beta=1}^M \tilde{G}_\beta(\boldsymbol{\sigma}_P) \psi_\beta(\mathbf{r}_P) e^{i\mathbf{k}_\beta \cdot \boldsymbol{\sigma}_P}, \quad (8)$$

where indices  $\alpha$  and  $\beta$  correspond to states where the electron is associated with the target and projectile centers, respectively. The momentum of the projectile ion, relative to the target atom in state  $\alpha$ , is given by  $\mathbf{k}_\alpha$ , and similarly the relative momentum of the projectile ion-electron system in state  $\beta$  with respect to the residual target proton is given by  $\mathbf{k}_\beta$ . The quantities  $\tilde{F}_\alpha$  and  $\tilde{G}_\beta$  are initially unknown expansion coefficients.

The interaction each center experiences with the active electron is spherically symmetric. In the case of the target proton this is described by the exact Coulomb potential, whereas for the projectile ion we approximate the interaction using  $V_{\text{mod}}$  in Eq. (6). Therefore, all pseudostates  $\psi_{\alpha(\beta)}$  are separable in radial and angular parts as

$$\psi_\alpha(\mathbf{r}) = R_{n_\alpha \ell_\alpha}(r) Y_{\ell_\alpha m_\alpha}(\hat{\mathbf{r}}), \quad (9)$$

where  $R_{n_\alpha \ell_\alpha}$  ( $R_{n_\beta \ell_\beta}$ ) is the radial wave function and  $Y_{\ell_\alpha m_\alpha}$  ( $Y_{\ell_\beta m_\beta}$ ) is a spherical harmonic. We use the true negative-energy eigenstates to describe the bound-state structure of the target. For the ion formed after the active electron is transferred to the projectile, we construct effective one-electron bound pseudostates by numerically solving Eq. (7) using the Numerov method. The first few orbital energies obtained in this work for the  $\text{C}^{2+} + e^-$  and  $\text{C}^{3+} + e^-$  systems are compared with the spectral data from NIST [56] in Table I. Here one can see that the obtained orbital energies are in reasonably good agreement with the recommended data.

In this approach we do not consider different spin states of the formed projectile ion after capture. Instead we generate states with the same spin that corresponds to the ground state of the outermost electron. This is particularly important for  $\text{C}^{3+} + \text{H}(1s)$  collisions, where it is possible for the  $\text{C}^{2+}$  ion to form through EC in either a singlet or triplet state. As we treat the projectile ion to be a structureless particle that interacts with the target electron and proton through  $V_{\text{mod}}$ , we are unable to differentiate the final spin states of the formed  $\text{C}^{2+}$  ion. Indeed, in principle it is possible to also generate states with energies resembling those of the triplet configurations by altering the model potential parameters. However, incorporating both of these sets of pseudostates into the expansion of the scattering wave function leads to the question of what set of parameters do we use to define  $V_{\text{mod}}$  when constructing the

TABLE I. Orbital energies (in a.u.) of single-electron states of  $C^{2+}$  and  $C^+$ . The present results, obtained by solving the E1E radial Schrödinger equation (7), are shown alongside energies from NIST [56]. Only the outermost electron is considered active while the inner electrons are frozen in their ground-state configuration.

$C^{2+}(1s^2 2s n\ell)$			$C^+(1s^2 2s^2 n\ell)$		
State	Present	NIST	State	Present	NIST
2s	-1.6941	-1.7598			
2p	-1.3672	-1.2935	2p	-0.9050	-0.8961
3s	-0.6439	-0.6337	3s	-0.3656	-0.3651
3p	-0.5640	-0.5800	3p	-0.3026	-0.2959
3d	-0.5038	-0.5000	3d	-0.2250	-0.2329
4s	-0.3384	-0.3395	4s	-0.1785	-0.1797
4p	-0.3073	-0.2907	4p	-0.1559	-0.1556
4d	-0.2833	-0.2826	4d	-0.1265	-0.1300
4f	-0.2813	-0.2895	4f	-0.1250	-0.1261

scattering potentials in Eqs. (4) and (5). We emphasize though that accounting for both singlet and triplet states individually should only become important at low energies, close 1 keV/u, which is the lowest projectile energy considered in this work.

In addition to the negative-energy bound states, there is a positive-energy continuum state. For the hydrogen atom, the continuum solution is known analytically to be the Coulomb wave whereas, for the dressed ion projectiles, the Coulomb-like wave is obtained through numerically solving Eq. (7) for a given ejected-electron energy. However, the continuum solution is not square integrable. To overcome this issue, we incorporate the wave-packet (WP) continuum-discretization approach, which was first outlined in Refs. [47,57]. Briefly, we subdivide the continuum in momentum space into a number of bins. Then WP pseudostates are generated by integrating the Coulomb or Coulomb-like wave functions over each bin. In this approach the total scattering wave function (8) is expanded using the true negative-energy eigenstates and positive-energy WP pseudostates around the target center as well as the negative-energy and positive-energy WP pseudostates around the projectile center. It is worth noting that all basis states belonging to the same center are orthonormal to each other. However, we do not require basis functions from one center to be orthogonal to basis functions belonging to the other center.

To formulate the close-coupling equations we begin by substituting the expansion of the total scattering wave function  $\Psi_i^+$  given in Eq. (8) into the TISE (1). After some lengthy algebra we apply the semiclassical approximation. Specifically, we use the impact-parameter description whereby the target proton is fixed at the origin and the projectile ion moves along a straight-line trajectory given by  $R(t, \mathbf{b}) = \mathbf{b} + \mathbf{v}t$ . Here  $\mathbf{b}$  is the impact parameter,  $t$  is time, and  $\mathbf{v}$  is the projectile velocity which is orientated entirely along the  $z = vt$  axis. Prior to the collision we have  $t = -\infty$  and  $t = 0$  corresponds to the closest approach of the projectile ion. This approximation brings temporal dependence into the picture and allows us to write  $\tilde{F}_\alpha(\sigma_T) \approx F_\alpha(t, \mathbf{b})$  and  $\tilde{G}_\beta(\sigma_P) \approx G_\beta(t, \mathbf{b})$ . Finally, we

obtain the set of coupled first-order differential equations

$$i\dot{F}_{\alpha'} + i \sum_{\beta=1}^M \dot{G}_\beta K_{\alpha'\beta}^T = \sum_{\alpha=1}^N F_\alpha D_{\alpha'\alpha}^T + \sum_{\beta=1}^M G_\beta Q_{\alpha'\beta}^T,$$

$$i \sum_{\alpha=1}^N \dot{F}_\alpha K_{\beta'\alpha}^P + i\dot{G}_{\beta'} = \sum_{\alpha=1}^N F_\alpha Q_{\beta'\alpha}^P + \sum_{\beta=1}^M G_\beta D_{\beta'\beta}^P, \quad (10)$$

$$\alpha' = 1, 2, \dots, N, \quad \beta' = 1, 2, \dots, M$$

for the expansion coefficients  $F_\alpha$  and  $G_\beta$ . Dots over the coefficients denote their time derivatives. Here the direct-scattering matrix elements are defined as

$$D_{\alpha'\alpha}^T(\mathbf{R}) = \langle \psi_{\alpha'} | \bar{V}_T | \psi_\alpha \rangle e^{i(\varepsilon_{\alpha'} - \varepsilon_\alpha)t},$$

$$D_{\beta'\beta}^P(\mathbf{R}) = \langle \psi_{\beta'} | \bar{V}_P | \psi_\beta \rangle e^{i(\varepsilon_{\beta'} - \varepsilon_\beta)t}, \quad (11)$$

where  $\varepsilon_\alpha$  and  $\varepsilon_\beta$  are the energies of the active electron in the  $\alpha$  target channel and  $\beta$  projectile channel, respectively. The overlap matrix elements are given as

$$K_{\alpha'\beta}^T(\mathbf{R}) = \langle \psi_{\alpha'} | e^{i\mathbf{v}\cdot\mathbf{r}_T} | \psi_\beta \rangle \exp[i(-v^2/2 + \varepsilon_{\alpha'} - \varepsilon_\beta)t],$$

$$K_{\beta'\alpha}^P(\mathbf{R}) = \langle \psi_{\beta'} | e^{-i\mathbf{v}\cdot\mathbf{r}_P} | \psi_\alpha \rangle \exp[i(-v^2/2 + \varepsilon_{\beta'} - \varepsilon_\alpha)t] \quad (12)$$

and the electron-transfer matrix elements are given by

$$Q_{\alpha'\beta}^T(\mathbf{R}) = \langle \psi_{\alpha'} | e^{i\mathbf{v}\cdot\mathbf{r}_T} (H_P + \bar{V}_P - \varepsilon_\beta) | \psi_\beta \rangle$$

$$\times \exp[i(-v^2/2 + \varepsilon_{\alpha'} - \varepsilon_\beta)t],$$

$$Q_{\beta'\alpha}^P(\mathbf{R}) = \langle \psi_{\beta'} | e^{-i\mathbf{v}\cdot\mathbf{r}_P} (H_T + \bar{V}_T - \varepsilon_\alpha) | \psi_\alpha \rangle$$

$$\times \exp[i(-v^2/2 + \varepsilon_{\beta'} - \varepsilon_\alpha)t]. \quad (13)$$

The close-coupling equations are solved using the initial condition

$$F_\alpha(-\infty, \mathbf{b}) = \delta_{\alpha,i}, \quad \alpha = 1, \dots, N$$

$$G_\beta(-\infty, \mathbf{b}) = 0, \quad \beta = 1, \dots, M, \quad (14)$$

which ensures the active electron is initially bound to the target proton in channel  $i$ . In this work we set  $i = 1$ , which corresponds to the ground state of H. In the limit as  $t \rightarrow +\infty$  the expansion coefficients  $F_\alpha$  and  $G_\beta$  represent the scattering amplitudes in the impact-parameter representation for transitions into channels  $\alpha$  and  $\beta$ , respectively. Therefore, solving the system of equations for  $F_\alpha$  and  $G_\beta$  and taking  $t \rightarrow +\infty$ , the state-resolved cross sections for direct scattering and electron capture can be determined.

## B. Evaluation of the scattering matrix elements

Here we provide details of evaluations of the scattering matrix elements (11)–(13). In particular, we focus on the modifications to the matrix elements that appear due to the inclusion of  $V_{\text{mod}}$  within potentials  $\bar{V}_T$  and  $\bar{V}_P$ .

Let us begin by considering the integral within the direct-scattering matrix elements for  $\beta \rightarrow \beta'$  transitions

$$\langle \psi_{\beta'} | \bar{V}_P | \psi_\beta \rangle = \delta_{\beta'\beta} V_{\text{mod}}(R) - \int d\mathbf{r}_P \psi_{\beta'}^*(\mathbf{r}_P) \frac{1}{r_P} \psi_\beta(\mathbf{r}_P). \quad (15)$$

Since  $r_T = |\mathbf{r}_P + \mathbf{R}|$ , the Coulomb interaction can be expanded in spherical harmonics with expansion coefficients

$$\mathcal{U}_\lambda(R, r_P) = \frac{[\min(R, r_P)]^\lambda}{[\max(R, r_P)]^{\lambda+1}}. \quad (16)$$

Separating the radial and angular parts of the pseudostates  $\psi_{\beta'}$  and  $\psi_\beta$  and substituting the expansion of the Coulomb interaction into Eq. (15), we get

$$\begin{aligned} \langle \psi_{\beta'} | \bar{V}_P | \psi_\beta \rangle &= \delta_{\beta'\beta} V_{\text{mod}}(R) - \sum_{\lambda\mu} \frac{4\pi(-1)^\lambda}{2\lambda+1} Y_{\lambda\mu}^*(\hat{\mathbf{R}}) \\ &\times \int dr_P r_P^2 R_{n_{\beta'}\ell_{\beta'}}(r_P) R_{n_\beta\ell_\beta}(r_P) \mathcal{U}_\lambda(R, r_P) \\ &\times \int d\hat{\mathbf{r}}_P Y_{\lambda\mu}(\hat{\mathbf{r}}_P) Y_{\ell_{\beta'}m_{\beta'}}^*(\hat{\mathbf{r}}_P) Y_{\ell_\beta m_\beta}(\hat{\mathbf{r}}_P). \end{aligned} \quad (17)$$

The angular integral can be taken analytically. As a result, Eq. (17) simplifies to

$$\begin{aligned} \langle \psi_{\beta'} | \bar{V}_P | \psi_\beta \rangle &= \delta_{\beta'\beta} V_{\text{mod}}(R) - \sum_{\lambda\mu} \sqrt{\frac{4\pi(2\ell_\beta+1)}{(2\ell_{\beta'}+1)(2\lambda+1)}} \\ &\times (-1)^{\ell_{\beta'}+\ell_\beta} C_{\ell_\beta 0 \lambda 0}^{\ell_{\beta'} 0} C_{\ell_\beta m_\beta \lambda \mu}^{\ell_{\beta'} m_{\beta'}} Y_{\lambda\mu}^*(\hat{\mathbf{R}}) \\ &\times \int dr_P r_P^2 R_{n_{\beta'}\ell_{\beta'}}(r_P) R_{n_\beta\ell_\beta}(r_P) \mathcal{U}_\lambda(R, r_P), \end{aligned} \quad (18)$$

where  $C_{\ell m \lambda \mu}^{\ell' m'}$  are the Clebsch-Gordan coefficients. The radial part of the integral is left to be evaluated numerically.

We follow the same procedure to derive the direct-scattering matrix elements for  $\alpha \rightarrow \alpha'$  transitions. However, in this case the form of the potential between the active electron and the projectile ion is no longer purely Coulombic. There are two additional terms present in the potential that screen the Coulomb attraction between the active electron and the projectile nucleus. These screening terms approximate the shielding effects of the frozen electrons on the projectile center. Therefore, after expressing  $r_P = |\mathbf{r}_T - \mathbf{R}|$ , we must also expand the exponential factors that are present in Eq. (6) as

$$\frac{e^{-\zeta|\mathbf{r}_T-\mathbf{R}|}}{|\mathbf{r}_T-\mathbf{R}|} = -4\pi\zeta \sum_{\lambda\mu} \mathcal{V}_\lambda(R, r_T) Y_{\lambda\mu}^*(\hat{\mathbf{R}}) Y_{\lambda\mu}(\hat{\mathbf{r}}_T) \quad (19)$$

and

$$e^{-\zeta|\mathbf{r}_T-\mathbf{R}|} = 2\pi \sum_{\lambda\mu} \mathcal{F}_\lambda(R, r_T) Y_{\lambda\mu}^*(\hat{\mathbf{R}}) Y_{\lambda\mu}(\hat{\mathbf{r}}_T). \quad (20)$$

The expansion coefficients  $\mathcal{V}_\lambda$  in Eq. (19) are given by

$$\mathcal{V}_\lambda(R, r_T) = \begin{cases} j_\lambda(i\zeta R) h_\lambda^{(1)}(i\zeta r_T) & \text{if } R \leq r_T \\ j_\lambda(i\zeta r_T) h_\lambda^{(1)}(i\zeta R) & \text{otherwise,} \end{cases} \quad (21)$$

where  $j_\lambda$  and  $h_\lambda^{(1)}$  denote the spherical Bessel and spherical Hankel functions of the first kind, respectively. Following the same approach as in Ref. [58], we evaluate these functions using the COULCC subroutine by Thompson and Barnett [59].

The expansion coefficients  $\mathcal{F}_\lambda$  present in Eq. (20) are given by

$$\mathcal{F}_\lambda(R, r_T) = \int_{-1}^1 dz \exp(-\zeta\sqrt{R^2+r_T^2-2Rr_Tz}) P_\lambda(z), \quad (22)$$

where  $z = \hat{\mathbf{r}}_T \cdot \hat{\mathbf{R}}$  and  $P_\lambda$  are the Legendre polynomials. These coefficients are calculated numerically. However, evaluating these integrals accurately is especially difficult given the singularitylike behavior that can appear at the boundary ( $z = 1$ ). For this reason, we employ the tanh-sinh quadrature method [60], which is designed to handle integrals with singularities or infinite derivatives at the boundaries. Using Eqs. (19) and (20), we now expand  $V_{\text{mod}}(r_P)$  as

$$V_{\text{mod}}(r_P) = \sum_{\lambda\mu} \frac{4\pi}{2\lambda+1} \mathcal{J}_\lambda(R, r_T) Y_{\lambda\mu}^*(\hat{\mathbf{R}}) Y_{\lambda\mu}(\hat{\mathbf{r}}_T), \quad (23)$$

where

$$\begin{aligned} \mathcal{J}_\lambda(R, r_T) &= q_P \mathcal{U}_\lambda(R, r_T) + \zeta(q_P - Z_P)(2\lambda+1) \mathcal{V}_\lambda(R, r_T) \\ &+ \frac{k}{2}(2\lambda+1) \mathcal{F}_\lambda(R, r_T). \end{aligned} \quad (24)$$

As done before, the angular part of  $\langle \psi_{\alpha'} | \bar{V}_T | \psi_\alpha \rangle$  is evaluated analytically in terms of the Clebsch-Gordan coefficients, leading to the final expression for the integral appearing in the  $\alpha \rightarrow \alpha'$  direct-scattering matrix elements

$$\begin{aligned} \langle \psi_{\alpha'} | \bar{V}_T | \psi_\alpha \rangle &= \delta_{\alpha'\alpha} V_{\text{mod}}(R) - \sum_{\lambda\mu} \sqrt{\frac{4\pi(2\ell_\alpha+1)}{(2\ell_{\alpha'}+1)(2\lambda+1)}} \\ &\times C_{\ell_\alpha 0 \lambda 0}^{\ell_{\alpha'} 0} C_{\ell_\alpha m_\alpha \lambda \mu}^{\ell_{\alpha'} m_{\alpha'}} Y_{\lambda\mu}^*(\hat{\mathbf{R}}) \\ &\times \int dr_T r_T^2 R_{n_{\alpha'}\ell_{\alpha'}}(r_T) R_{n_\alpha\ell_\alpha}(r_T) \mathcal{J}_\lambda(R, r_T). \end{aligned} \quad (25)$$

The overlap (12) and rearrangement (13) matrix elements are evaluated in spheroidal coordinates where the azimuthal component of the integral is calculated analytically in terms of the Bessel functions. The remainder of the integral is evaluated numerically using the Gauss-Laguerre and Gauss-Legendre quadrature rules. Therefore, no significant changes need to be made when incorporating the model potential. The details regarding this method of evaluating the overlap and rearrangement matrix elements are provided in Ref. [61].

### III. DETAILS OF CALCULATIONS

The close-coupling equations (10) are solved numerically using the Runge-Kutta method along a discretized  $z$  grid in the interval  $[-z_{\text{max}}, z_{\text{max}}]$  with a sufficient number of points. Setting  $z_{\text{max}} = 150$  a.u. and  $z_{\text{max}} = 175$  a.u. gives negligible differences in the results. Therefore, we set  $z_{\text{max}} = 175$  a.u. for all calculations. For both collision systems, the number of points used to construct the  $z$  grid ranges from 600 to 4000 depending on the projectile energy. We find that more points are required at the lower energies compared to the higher ones in order to achieve stable results. However, across the entire projectile energy range, the overall uncertainty in the obtained results with respect to the number of time steps is kept below 0.1%.

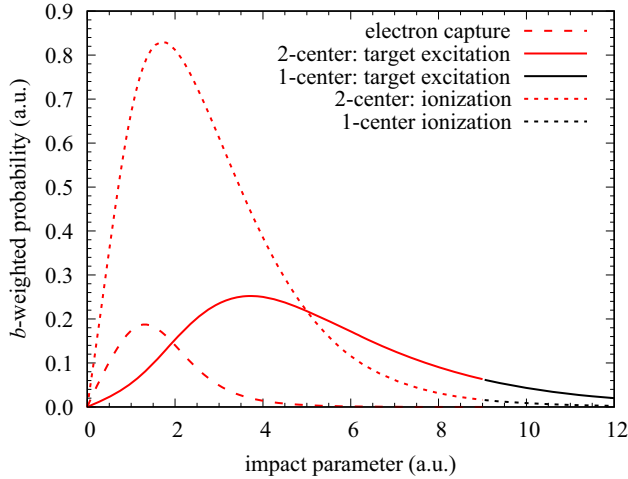


FIG. 1. Weighted probability distributions for total electron capture, target excitation, and ionization in  $C^{2+} + H(1s)$  collisions at the projectile energy of 100 keV/u. Results are shown only up to an impact parameter of 12 a.u.; however, these calculations extend to 25 a.u.

At energies below 30 keV/u, our impact-parameter grid ranges from 0 to 14 a.u. Much like the  $z$  grid, the number of impact-parameter points required depends on the projectile energy. At lower energies a total of 128 impact-parameter points are needed to resolve the structures that appear in the probabilities. This number is systematically decreased to 64 points at 30 keV/u. At energies above 30 keV/u, we find the impact-parameter range needed for the target-excitation and direct-ionization processes is much larger than that needed for both EC into bound states and EC into the continuum of the projectile [53]. Therefore, in this work we employ two-center calculations up to an impact parameter  $b_{\max}^{2c}$  where all EC probabilities have fallen at least three orders of magnitude. These calculations are then extended by performing one-center calculations up to some larger impact parameter  $b_{\max}^{1c}$ . We then integrate over the entire combined  $b$ -weighted probability distributions to obtain the total ionization and target-excitation cross sections. Figure 1 demonstrates this approach by showing the weighted probabilities for electron capture, target excitation, and ionization in  $C^{2+} + H(1s)$  collisions at 100 keV/u projectile energy. The red lines indicate the two-center calculations, whereas the black lines represent the one-center ones. Here we see that the two-center and one-center probabilities join seamlessly.

For further details regarding this approach, see Ref. [53]. At projectile energies above 30 keV/u, the largest  $b_{\max}^{2c}$  needed is 13 a.u., whereas the largest  $b_{\max}^{1c}$  necessary is 50 a.u.

The quality of the final results obtained using close-coupling approaches also depends on the basis size. The structure of our basis is described using three parameters. These are the maximum principal quantum number of bound states included  $n_{\max}$ , the maximum angular momentum quantum number of all included states  $\ell_{\max}$ , and the number of pseudocontinuum WP states included  $n_c$ . For both  $C^{2+} + H(1s)$  and  $C^{3+} + H(1s)$  collision systems, we fix  $n_{\max} = 12$  and  $n_c = 18$  at all energies considered in this work. However, we vary  $\ell_{\max}$  with increasing projectile energy to ensure that

approximately the same degree of convergence is maintained. At lower energies we use  $\ell_{\max} = 7$  for both collision systems, whereas at higher incident energies we set  $\ell_{\max} = 5$ . Thus, the largest basis size used in our calculations is 3224 states. All the cross sections presented in this work have converged within a few percent.

Ill-conditioning effects in calculations can appear when establishing convergence in results with increasing basis size due to the nonorthogonality of the underlying basis. These effects are diminished when evaluating the scattering matrix elements with sufficiently high precision. In this work we extend the radial grid used to evaluate the direct matrix elements in Eqs. (18) and (25) to 400 a.u., using up to 5500 quadrature points. We also use a maximum of 320 Gauss-Laguerre and 320 Gauss-Legendre quadrature points to calculate the overlap and electron-transfer matrix elements. The number of Gauss-Laguerre and Gauss-Legendre quadrature points used depends on the projectile energy. This is due to the fact that these matrix elements contain an oscillatory factor in the integrand which depends on the projectile speed. Therefore, the largest number of quadrature points used is at 1 MeV/u, the largest incident energy considered.

#### IV. RESULTS AND DISCUSSION

In this section we present results for the total electron-capture, ionization, and target-excitation cross sections in  $C^{2+} + H(1s)$  and  $C^{3+} + H(1s)$  collisions. Furthermore, we present the partial electron-capture and target-excitation cross sections into the  $n = 2$  and 3 states. We compare our results to experimental measurements and other theoretical calculations where available. In all figures below, we present our calculations with points connected by straight lines to guide the eye of the reader. The incident energies at which we have performed calculations were chosen to best represent any structures in the cross sections.

Figure 2 presents the WP-CCC results for the total cross section for electron capture in  $C^{2+} + H(1s)$  collisions alongside the experimental [16–19] and other theoretical [46] data. Above 20 keV/u, the present results are in excellent agreement with the measurements by Phaneuf *et al.* [17] and Goffe *et al.* [18]. Between 8 and 20 keV/u, the two sets of experimental data appear to display contradictory behaviors. The results by Goffe *et al.* show an increase in the cross section within the energy range from about 8 to 15 keV/u, whereas the measurements by Phaneuf *et al.* suggest it declines. However, the WP-CCC results display a local minimum at about 12 keV/u. Therefore, this apparent disagreement in the behavior of the cross section between the two sets of experiments may simply be due to the lack of measurements in the energy range from 10 to 15 keV/u. Our results agree better with the data by Goffe *et al.* around 8 keV/u; however, we see better agreement with the measurements by Phaneuf *et al.* at 15 keV/u. Some disagreement is seen when comparing the WP-CCC results to the BCIS ones by Sounda *et al.* [46] from 50 to 200 keV/u where the latter are available. A possible reason for this discrepancy is that the BCIS method does not account for the coupling between the channels, which is important to obtain accurate results in the intermediate-energy region.

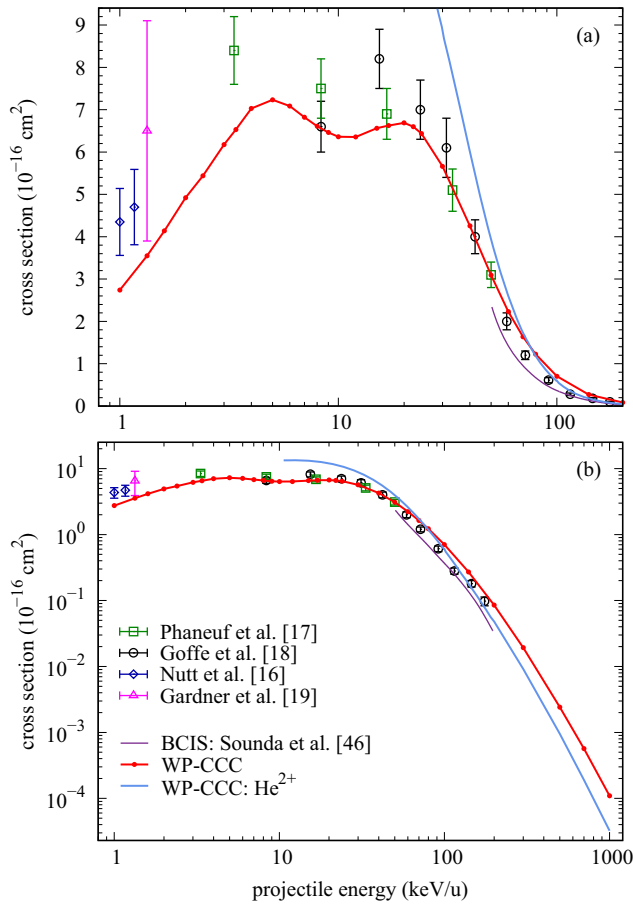


FIG. 2. Total cross section for electron capture in  $C^{2+} + H(1s)$  collisions, using (a) linear and (b) logarithmic scales. The experimental data are from Goffe *et al.* [18], Phaneuf *et al.* [17], Nutt *et al.* [16], and Gardner *et al.* [19]. Theoretical results include the present WP-CCC calculations and BCIS calculations by Sounda *et al.* [46]. The WP-CCC results for  $He^{2+} + H(1s)$  collisions by Faulkner *et al.* [49] are also shown. The legend in (b) applies to both panels.

The energy dependence of the total electron-capture cross section for  $C^{3+} + H(1s)$  collisions is shown in Fig. 3. Alongside the WP-CCC results, the experimental [15,17,18,21] and other theoretical [30,40,41,45] data are shown. We find excellent agreement with measurements by Phaneuf *et al.* [17] across the entire projectile-energy range where the latter are available. Furthermore, excluding the measurement at about 12 keV/u, the WP-CCC results agree well with the experimental data by Goffe *et al.* [18]. The AOCC calculations by Tseng and Lin [45] show a noticeable difference in the functional behavior of the EC cross section below 30 keV/u. Nevertheless, for  $C^{3+} + H(1s)$  collisions, we see improved agreement between the WP-CCC results and the BCIS ones, compared to the case for the  $C^{2+} + H(1s)$  system. Between 10 and 20 keV/u the WP-CCC results disagree with the CTMC calculations by Errea *et al.* [41]. However, above 20 keV/u the two sets of calculations converge to each other. We find excellent agreement with the TC-BGM results by Leung and Kirchner [30] across the energy range from 1 to 100 keV/u where the latter are available.

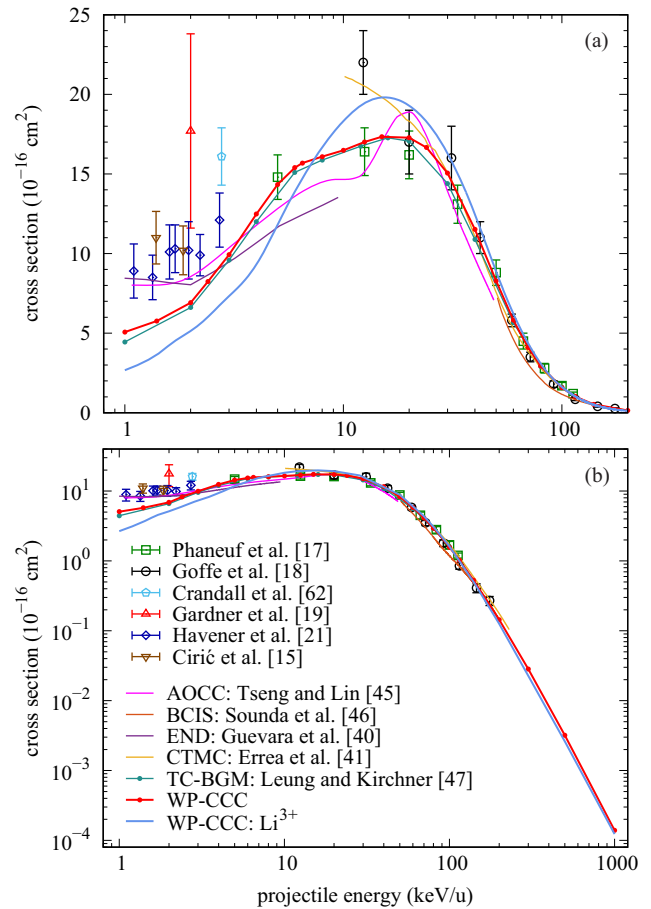


FIG. 3. Total cross section for electron capture in  $C^{3+} + H(1s)$  collisions, using (a) linear and (b) logarithmic scales. The experimental data are from Goffe *et al.* [18], Crandall *et al.* [62], Phaneuf *et al.* [17], Havener *et al.* [21], and Ćirić *et al.* [15]. Theoretical results include the present WP-CCC calculations, AOCC calculations by Tseng and Lin [45], END method by Guevara *et al.* [40], CTMC calculations by Errea *et al.* [41], and TC-BGM results by Leung and Kirchner [30]. The WP-CCC results for  $Li^{3+} + H(1s)$  collisions by Kotian *et al.* [50] are also shown. The legend in (b) applies to both panels.

As one can see in Figs. 2 and 3, at projectile energies below 5 keV/u, the WP-CCC results for the total EC cross section underestimate the available measurements. Experimental data from Ćirić *et al.* [15] and McCullough *et al.* [13] along with MOCC calculations by Errea *et al.* [39] for the state-resolved cross sections show that, at low energies, two-electron processes have a significant contribution to the total EC cross section. Specifically, it is found that the transitions where the target electron is captured into the  $2p$  shell of the projectile and one of the projectile electrons is simultaneously excited to the  $2p$  state can contribute up to 35% of the total EC cross section. The WP-CCC approach presented here is based on an effective one-electron description of the collision problem. Therefore, our results do not include contributions from two-electron processes at this stage. For this reason the present WP-CCC results for EC underestimate the experimental data. It is also worth mentioning that given the significant role the two-electron processes play in the total EC cross

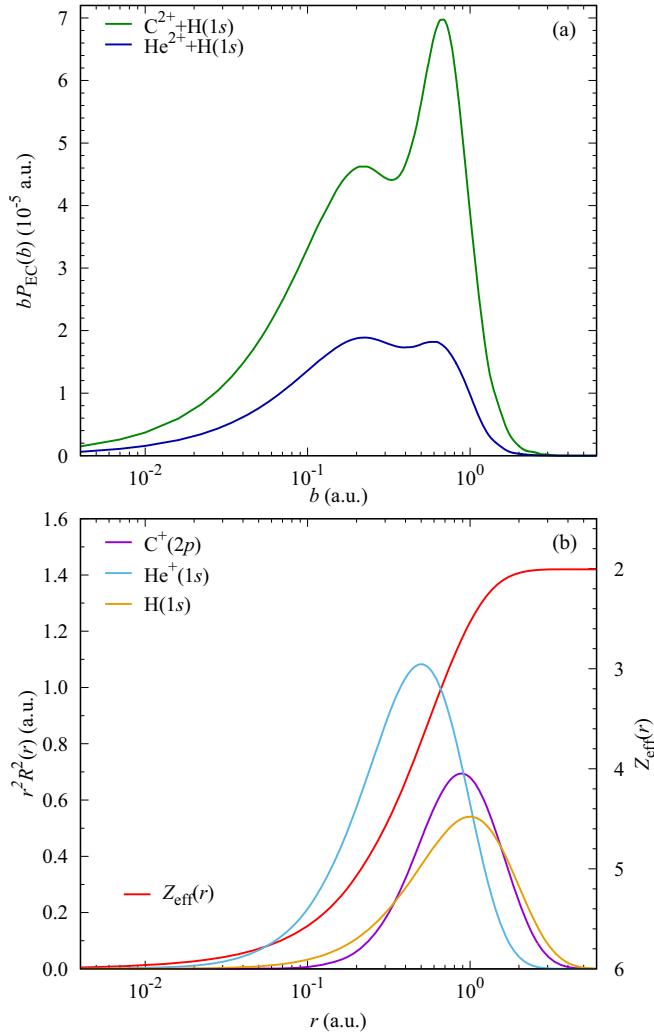


FIG. 4. (a) Impact-parameter weighted probabilities for total electron capture in  $\text{C}^{2+} + \text{H}(1s)$  and  $\text{He}^{2+} + \text{H}(1s)$  collisions at an incident energy of 1 MeV/u. (b) Radial dependence of the projectile effective charge  $Z_{\text{eff}}$  and the electron probability densities for  $\text{H}(1s)$ ,  $\text{He}^+(1s)$ , and  $\text{C}^+(2p)$ .

section at low energies, coupling to these channels should also be important.

To understand the effect the projectile electrons have on the total EC cross section in  $\text{C}^{2+}$  and  $\text{C}^{3+}$  collisions with H, in Figs. 2 and 3 we also present the WP-CCC results for the total EC cross section in  $\text{He}^{2+} + \text{H}(1s)$  [49] and  $\text{Li}^{3+} + \text{H}(1s)$  [50] collisions, respectively. It is not surprising that the results for  $\text{C}^{2+} + \text{H}(1s)$  and  $\text{He}^{2+} + \text{H}(1s)$  collisions differ at low energies. However, Fig. 2 shows that, starting at about 100 keV/u, the total EC cross section for  $\text{C}^{2+} + \text{H}(1s)$  collisions becomes increasingly larger than the one for  $\text{He}^{2+} + \text{H}(1s)$  collisions. The reason for this is related to (i) the radial probability distribution for finding the electron of the H target and (ii) the projectile–target–electron interaction. To show this, in Fig. 4(a) we present the impact-parameter dependence of the weighted probabilities for EC in both  $\text{C}^{2+} + \text{H}(1s)$  and  $\text{He}^{2+} + \text{H}(1s)$  collisions at a collision energy of 1 MeV/u. Furthermore, in Fig. 4(b) we show the radial dependence of the target-electron probability density and the projectile

effective charge  $Z_{\text{eff}}(r)$ . Here we define the effective charge  $Z_{\text{eff}}(r)$  as the radius-weighted model potential, i.e.,  $Z_{\text{eff}}(r) = rV_{\text{mod}}(r)$ . The figure shows that at values of  $r \equiv r_p$  on the order of the impact parameter where EC is most likely to occur for both systems, the target electron is more attracted to the  $\text{C}^{2+}$  ion than the  $\text{He}^{2+}$  one. Generally speaking, as the projectile energy increases, EC is more likely to occur at smaller impact parameters. Therefore, in  $\text{C}^{2+} + \text{H}(1s)$  collisions as the incident energy increases the target electron is able to approach the bare carbon nucleus more closely. This results in a stronger attraction to the carbon ion than to the bare helium one. It is for these reasons the EC cross section for the  $\text{C}^{2+}$  is increasingly larger than for the  $\text{He}^{2+}$  one with increasing projectile energies. Comparing the total cross sections for EC in  $\text{C}^{3+} + \text{H}(1s)$  and  $\text{Li}^{3+} + \text{H}(1s)$  collisions shown in Fig. 3, we see smaller differences. In fact, up to 1 MeV/u incident energy the cross section for  $\text{C}^{3+} + \text{H}(1s)$  collisions is marginally larger than the one for  $\text{Li}^{3+} + \text{H}(1s)$  collisions. To explain this result, in Fig. 5(a) we present the impact-parameter weighted probability for EC in  $\text{C}^{3+} + \text{H}(1s)$  and  $\text{Li}^{3+} + \text{H}(1s)$  collisions at 1 MeV/u. Additionally, we present the radial dependence of the effective charge for the  $\text{C}^{3+}$  ion in Fig. 5(b), as was done in Fig. 4 for the  $\text{C}^{2+}$  ion. The figure shows that at radial distances on the order of the impact-parameter value where EC is most likely to occur, the  $\text{C}^{3+}$  ion has a greater effective charge than the charge of  $\text{Li}^{3+}$ . This leads to a larger EC cross section for  $\text{C}^{3+}$  collisions compared to  $\text{Li}^{3+}$  collisions. However, the difference between the effective charge of the  $\text{C}^{3+}$  ion in this region compared to the charge of  $\text{Li}^{3+}$  is smaller than the same for the  $\text{C}^{2+}$  and  $\text{He}^{2+}$  pair. This explains why the difference in the EC cross sections for  $\text{C}^{3+} + \text{H}(1s)$  and  $\text{Li}^{3+} + \text{H}(1s)$  collisions is smaller compared to the differences found for  $\text{C}^{2+}$  and  $\text{He}^{2+}$  collisions with  $\text{H}(1s)$ .

Another factor that contributes to the difference in the results for the dressed ion and the fully stripped ion of the corresponding charge is the  $Q$  value. The  $Q$  values are particularly important at low and intermediate energies. In part, this is why we see significant deviations between the corresponding systems at these energies. However, at high energies, where we compare the results for the dressed ion and the fully stripped ion of the corresponding charge, the  $Q$  values become less important. This is because at high energies, capture to the lowest-energy state available on the projectile becomes dominant regardless of the  $Q$  value. This has been demonstrated in the example of  $\text{Be}^{4+} + \text{H}(1s)$  collisions in Ref. [51] (see Fig. 3 of [51]) and  $\text{Ne}^{10+} + \text{H}(1s)$  collisions in Ref. [54] (see Fig. 4 of [54]).

The total cross sections for ionization in  $\text{C}^{2+} + \text{H}(1s)$  and  $\text{C}^{3+} + \text{H}(1s)$  collisions are shown in Figs. 6 and 7, respectively, in comparison with the measurements by Shah and Gilbody [22,23]. Ionization in the  $\text{C}^{3+} + \text{H}(1s)$  system has been calculated by Leung and Kirchner [30] using the TC-BGM. For  $\text{C}^{2+}$  scattering on H, the WP-CCC results significantly differ from the experimental data at all energies. At the same time, for  $\text{C}^{3+} + \text{H}(1s)$  collisions our calculations reasonably agree with the measurements between 20 and 50 keV/u. The TC-BGM results agree with the experiment slightly better; however, they are limited to energies below 100 keV/u. For both systems, at the energies where the cross



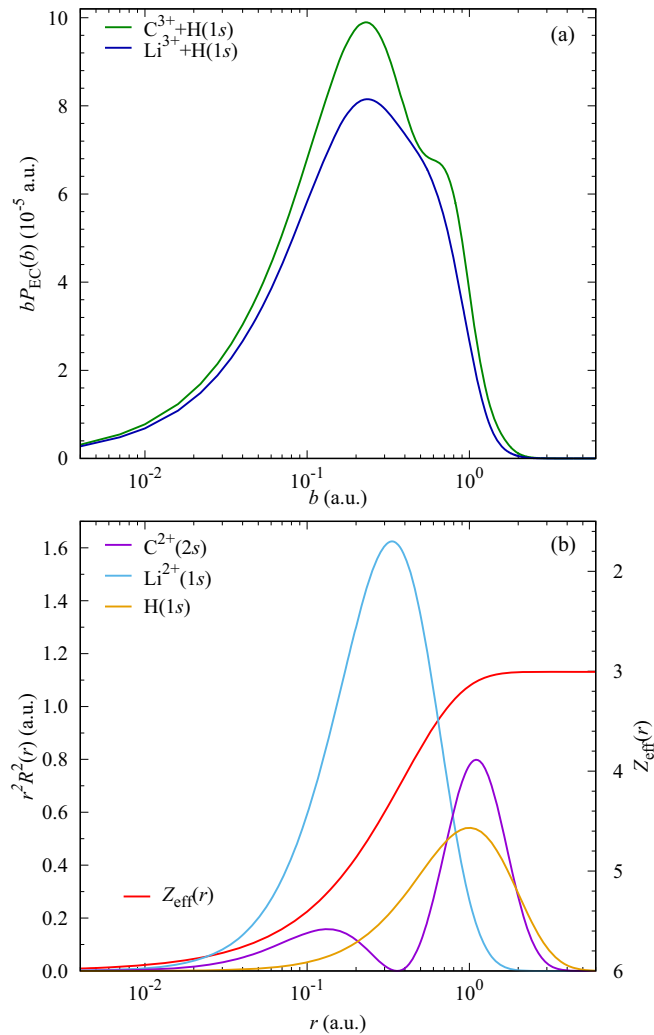


FIG. 5. (a) Impact-parameter weighted probabilities for total electron capture in  $C^{3+} + H(1s)$  and  $Li^{3+} + H(1s)$  collisions at an incident energy of 1 MeV/u. (b) Radial dependence of the projectile effective charge  $Z_{\text{eff}}$  and the electron probability densities for  $H(1s)$ ,  $Li^{2+}(1s)$ , and  $C^{2+}(2p)$ .

section peaks the present results deviate most from the experimental data. It is worth noting that this level of disagreement between close-coupling calculations and measurements performed by Shah and Gilbody is also found for the case of proton collisions with atomic hydrogen [63,64], which represents the simplest true three-body system. Whether there is an issue with the modeling of ionization within the two-center close-coupling framework or an inaccuracy in the measurements remains to be determined. We conclude that more experimental and theoretical work on ionization in these collisions is required.

As done for EC, in Figs. 6 and 7 we include the WP-CCC results for the total ionization cross section in  $He^{2+} + H(1s)$  and  $Li^{3+} + H(1s)$  collisions, respectively. It can be seen that the results for  $C^{2+}$  collisions are considerably larger than the ones for  $He^{2+}$  collisions across the entire projectile energy range. In particular, at energies below 30 keV/u we see that the  $C^{2+}$  projectile produces a cross section over a factor of 2 larger than the one in  $He^{2+} + H(1s)$  collisions.

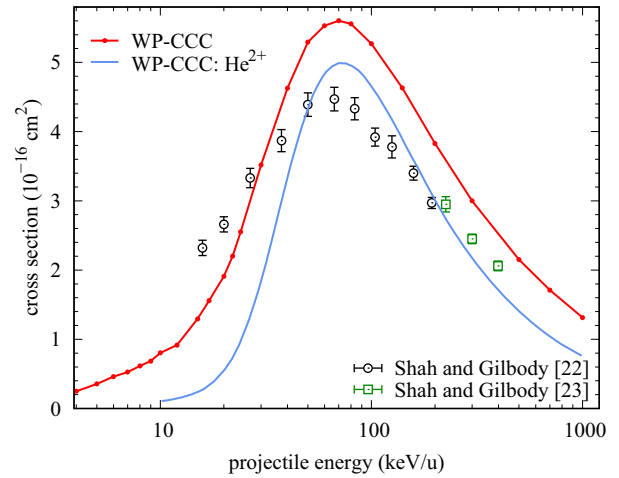


FIG. 6. Total cross section for ionization in  $C^{2+} + H(1s)$  collisions. The present WP-CCC calculations are compared with the experimental data by Shah and Gilbody [22,23]. The WP-CCC results for  $He^{2+} + H(1s)$  collisions by Faulkner *et al.* [49] are also shown.

However, despite the quantitative differences, we note that the functional behavior of both cross sections is similar for both collision systems at all incident energies. In contrast to the  $C^{2+}$  projectile, the difference in the ionization cross section for  $C^{3+} + H(1s)$  and  $Li^{3+} + H(1s)$  collisions appears to be quite small; however, as the projectile energy increases towards 1 MeV/u, the differences become visible.

The cross sections for target excitation into the  $n = 2$  and 3 states in  $C^{2+} + H(1s)$  and  $C^{3+} + H(1s)$  collisions are presented in Figs. 8 and 9, respectively. Also included in both figures is the projectile energy dependence of the total target-excitation cross section. Here we define the total target-excitation cross section as the sum of all state-selective cross sections for excitation up to the principal and angular

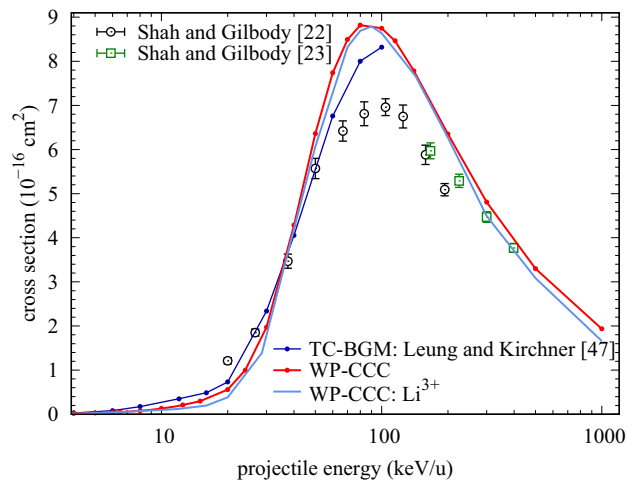


FIG. 7. Total cross section for ionization in  $C^{3+} + H(1s)$  collisions. The present WP-CCC calculations are compared with the experimental data from Shah and Gilbody [22,23] and the TC-BGM calculations by Leung and Kirchner [30]. The WP-CCC results for  $Li^{3+} + H(1s)$  collisions from Kotian *et al.* [50] are also shown.

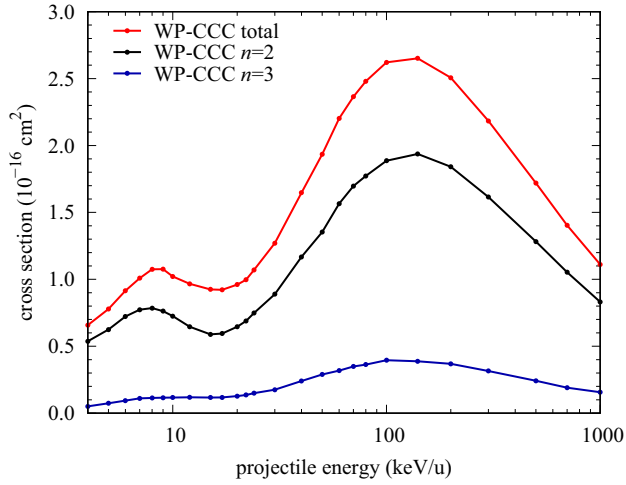


FIG. 8. The WP-CCC cross sections for target excitation into the  $n = 2$  and 3 states in  $C^{2+} + H(1s)$  collisions. The total target-excitation cross section is also shown.

momentum quantum numbers  $n_{\max}$  and  $\ell_{\max}$ , respectively, that we use to characterize our basis. Since our results are checked for convergence with respect to the size of the basis used to expand the scattering wave function, the remaining states give a negligible contribution. We see that for  $C^{3+}$  induced excitation of  $H(1s)$  into the  $n = 2$  and 3 states, the WP-CCC results and TC-BGM ones by Leung and Kirchner [30] agree well below 30 keV/u. However, above this energy the two sets of calculations begin to deviate from one another. Looking at the results for target excitation in both  $C^{2+}$  and  $C^{3+}$  ion collisions, we find that the cross section for total excitation is dominated by transitions to the  $n = 2$  states across the entire incident energy range considered in this work.

Figure 10 presents the first few  $n$ -partial cross sections for EC in  $C^{2+} + H(1s)$  collisions as a function of incident energy. Interestingly, we see that capture into the  $n = 2$  states is dominant between 1 and 10 keV/u and above 30 keV/u;

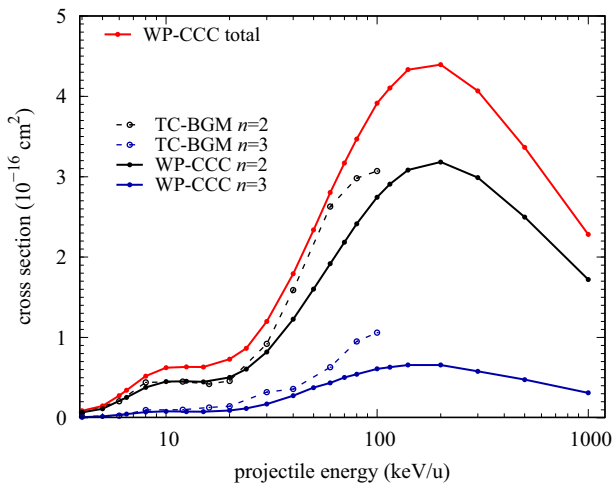


FIG. 9. The WP-CCC cross sections for target excitation into the  $n = 2$  and 3 states in  $C^{3+} + H(1s)$  collisions in comparison with the TC-BGM results by Leung and Kirchner [30]. The present total target-excitation cross section is also shown.

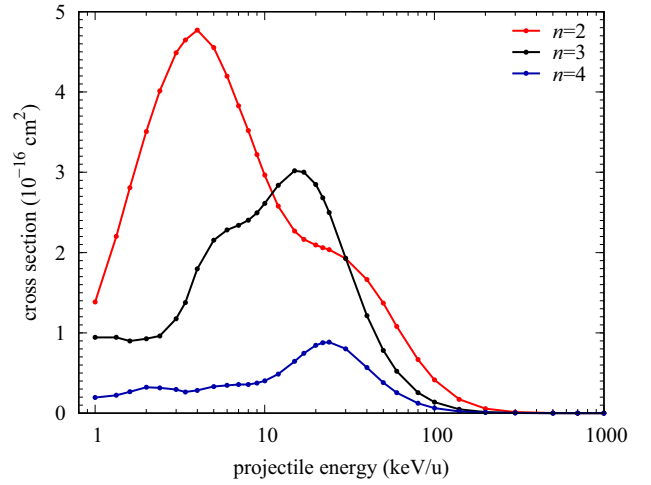


FIG. 10. The WP-CCC  $n$ -resolved cross sections for electron capture in  $C^{2+} + H(1s)$  collisions.

however, between 10 and 30 keV/u capture into the  $n = 3$  states dominates. Furthermore, the cross section for capture into the  $n = 2$  states peaks at about 4 keV/u and for  $n = 3$  at 20 keV/u. It is these different projectile energies where the cross section for EC into the  $n = 2$  and 3 states peaks that give rise to the saddle shape with a local minimum seen in the total EC cross section.

The  $n$ -resolved cross sections for EC in  $C^{3+} + H(1s)$  collisions are presented in Fig. 11. In contrast to the  $C^{2+}$  case where at energies below 100 keV/u the dominant capture channel oscillates between the  $n = 2$  and 3 states, for  $C^{3+}$  we find that EC into the  $n = 3$  states is largest everywhere. Further, we see that the cross section for EC into the  $n = 3$  states between 1 and 30 keV/u is over three times larger than the ones for EC into the  $n = 2$  and 4 states.

## V. CONCLUSION

The two-center WP-CCC approach was extended to dressed ion collisions with atomic hydrogen. A model po-

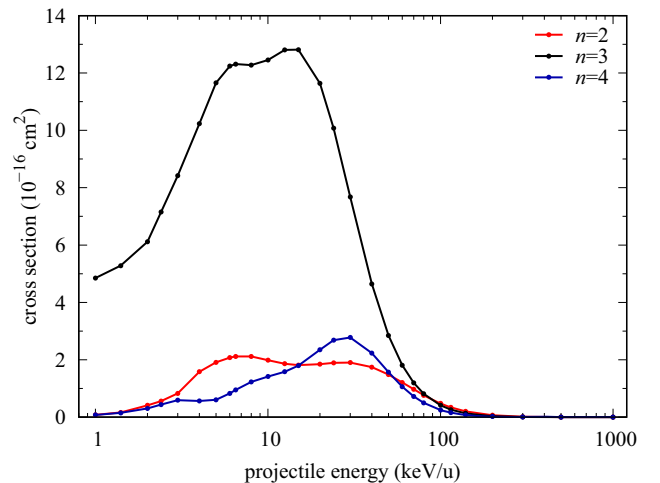


FIG. 11. Same as in Fig. 10 but for  $C^{3+} + H(1s)$  collisions.

tential was used to approximately describe the interaction of the incoming projectile ion with the target. This reduced the scattering problem to an effective three-body one with a single active electron. The method was applied to calculate the total and  $n$ -resolved cross sections for electron capture, target excitation, and ionization occurring in  $C^{2+} + H(1s)$  and  $C^{3+} + H(1s)$  collisions. The calculations were performed across a broad incident energy range from 1 keV/u to 1 MeV/u. To ensure the accuracy of our results (within the model), we performed stringent convergence tests with increasing basis size and numerical parameters. We compared the present calculations with the experimental data and previous theoretical results, where available. For both collision systems, our results were in excellent agreement with the available measurements for the total EC cross section above 5 keV/u; however, they underestimated the experimental data below 5 keV/u. One possible reason for this difference comes from the two-electron processes that our approach, at this stage, does not take into account. For the energy dependence of the total EC cross section in  $C^{2+} + H(1s)$  collisions, we provided theoretical results below 50 keV/u. This allowed us to compare theory with some of the experimental measurements for this process. To investigate the effect projectile electrons have on the total EC cross section in  $C^{2+} + H(1s)$  and  $C^{3+} + H(1s)$  collisions, we compared our results with those for  $He^{2+} + H(1s)$  [49] and  $Li^{3+} + H(1s)$  [50] collisions, respectively. We found that the  $C^{2+} + H(1s)$  results differ significantly from the  $He^{2+} + H(1s)$  ones across the entire projectile energy range considered. Furthermore, an increasingly larger cross section for EC in  $C^{2+}$  ion collisions was obtained than in the  $He^{2+}$  ones at energies above 100 keV/u. This was due to the fact that at higher energies, the projectile could approach the target electron closer, resulting in a stronger attraction to the carbon ion than the bare helium one. Similar observations were also made when comparing the total cross section for EC in  $C^{3+} + H(1s)$  collisions against

the one for  $Li^{3+} + H(1s)$  collisions. However, here the differences between the results were less than the ones between the  $C^{2+}$  and  $He^{2+}$  projectiles. Therefore, the difference in the corresponding cross sections was also smaller.

As to the ionization process, the present results generally overestimated experimental data by Shah and Gilbody [22,23]. We also found that the  $C^{2+}$  results are somewhat larger than those for the  $He^{2+}$  projectile and the  $C^{3+}$  results are slightly larger than the  $Li^{3+}$  ones, similar to the situation observed for EC. The reason for this may be similar as well. When the projectile comes close to the target, the active electron can penetrate deeper, experiencing a stronger attraction towards the projectile nucleus than at asymptotically large distances. This increases the probability of ionization.

In this work we showed that the WP-CCC method is capable of calculating the total and  $n$ -resolved cross sections for dressed ion collisions with hydrogen so long as the projectile energy is sufficiently large that two-electron processes can be ignored. The incorporation of this model potential into the WP-CCC approach for two-electron targets is left for future work [36]. This would allow us to study various dressed ion collisions with He. Further work could also incorporate a two-electron structure model for the dressed ion projectiles. This would allow us to study the spin-resolved partial cross sections, which are of importance in astrophysics.

All the data obtained in this work are available from the authors upon request.

#### ACKNOWLEDGMENTS

This work was supported by the Australian Research Council, the Pawsey Supercomputer Centre, and the National Computing Infrastructure. N.W.A. and C.T.P. acknowledge support through Australian Government Research Training Program Scholarships.

- 
- [1] N. A. Schwadron and T. E. Cravens, *Astrophys. J.* **544**, 558 (2000).
- [2] R. T. Zhang, T. Liao, C. J. Zhang, L. P. Zou, D. L. Guo, Y. Gao, L. Y. Gu, X. L. Zhu, S. F. Zhang, and X. Ma, *Mon. Not. R. Astron. Soc.* **520**, 1417 (2023).
- [3] Dž. Belkić, *J. Math. Chem.* **47**, 1366 (2010).
- [4] A. C. Kraan, *Front. Oncol.* **5**, 150 (2015).
- [5] M. Durante, J. Debus, and J. S. Loeffler, *Nat. Rev. Phys.* **3**, 777 (2021).
- [6] T. Liamsuwan and H. Nikjoo, *Phys. Med. Biol.* **58**, 641 (2013).
- [7] H. Nikjoo, S. Uehara, D. Emfietzoglou, and A. Brahme, *New J. Phys.* **10**, 075006 (2008).
- [8] O. Marchuk, *Phys. Scr.* **89**, 114010 (2014).
- [9] A. Kallenbach, R. Dux, J. C. Fuchs, R. Fischer, B. Geiger, L. Giannone, A. Herrmann, T. Lunt, V. Mertens, R. McDermott, R. Neu, T. Pütterich, S. Rathgeber, V. Rohde, K. Schmid, J. Schweinzer, W. Treutterer, and A. U. Team, *Plasma Phys. Control. Fusion* **52**, 055002 (2010).
- [10] R. Pitts, S. Carpentier, F. Escourbiac, T. Hirai, V. Komarov, A. Kukushkin, S. Lisgo, A. Loarte, M. Merola, R. Mitteau, A. Raffray, M. Shimada, and P. Stangeby, *J. Nucl. Mater.* **415**, S957 (2011).
- [11] R. C. Isler, *Plasma Phys. Control. Fusion* **36**, 171 (1994).
- [12] C. Hill, Dipti, K. Heinola, A. Dubois, N. Sisourat, A. Taoutioui, H. Agueny, K. Tőkési, I. Ziaecian, C. Illescas, A. Jorge, L. Méndez, A. Kadyrov, N. Antonio, A. Kotian, T. Kirchner, A. Leung, J. Ko, J. Lee, O. Marchuk *et al.*, *Nucl. Fusion* **63**, 125001 (2023).
- [13] R. W. McCullough, F. G. Wilkie, and H. B. Gilbody, *J. Phys. B: At. Mol. Phys.* **17**, 1373 (1984).
- [14] F. G. Wilkie, R. W. McCullough, and H. B. Gilbody, *J. Phys. B: At. Mol. Phys.* **19**, 239 (1986).
- [15] D. Čirić, A. Brazuk, D. Dijkkamp, F. J. de Heers, and H. Winter, *J. Phys. B: At. Mol. Phys.* **18**, 3629 (1985).
- [16] W. L. Nutt, R. W. McCullough, and H. B. Gilbody, *J. Phys. B: At. Mol. Phys.* **11**, L181 (1978).
- [17] R. A. Phaneuf, F. W. Meyer, and R. H. McKnight, *Phys. Rev. A* **17**, 534 (1978).
- [18] T. V. Goffe, M. B. Shah, and H. B. Gilbody, *J. Phys. B: At. Mol. Phys.* **12**, 3763 (1979).

- [19] L. D. Gardner, J. E. Bayfield, P. M. Koch, I. A. Sellin, D. J. Pegg, R. S. Peterson, and D. H. Crandall, *Phys. Rev. A* **21**, 1397 (1980).
- [20] R. A. Phaneuf, I. Alvarez, F. W. Meyer, and D. H. Crandall, *Phys. Rev. A* **26**, 1892 (1982).
- [21] C. C. Havener, A. Müller, P. A. Zeijlmans van Emmichoven, and R. A. Phaneuf, *Phys. Rev. A* **51**, 2982 (1995).
- [22] M. B. Shah and H. B. Gilbody, *J. Phys. B: At. Mol. Phys.* **14**, 2831 (1981).
- [23] M. B. Shah and H. B. Gilbody, *J. Phys. B: At. Mol. Phys.* **16**, 4395 (1983).
- [24] *State-of-the-Art Reviews on Energetic Ion-Atom and Ion-Molecule Collisions*, edited by Dž. Belkić, I. Bray, and A. Kadyrov (World Scientific, Singapore, 2019).
- [25] C. Harel, H. Jouin, and B. Pons, *At. Data Nucl. Data Tables* **68**, 279 (1998).
- [26] L. F. Errea, C. Harel, H. Jouin, L. Méndez, B. Pons, and A. Riera, *J. Phys. B: At. Mol. Opt. Phys.* **31**, 3527 (1998).
- [27] Dž. Belkić, S. Saini, and H. S. Taylor, *Phys. Rev. A* **36**, 1601 (1987).
- [28] D. R. Schultz and P. S. Krstic, *Atomic and Plasma-Material Interaction Data For Fusion* (IAEA, Vienna, 1997), Vol. 6, p. 173.
- [29] I. Ziaecian and K. Tőkési, *Atoms* **8**, 27 (2020).
- [30] A. C. K. Leung and T. Kirchner, *Atoms* **10**, 11 (2022).
- [31] T. G. Winter, *Phys. Rev. A* **25**, 697 (1982).
- [32] N. Toshima, *Phys. Rev. A* **50**, 3940 (1994).
- [33] H. Agueny, J. P. Hansen, A. Dubois, A. Makhoute, A. Taoutioui, and N. Sisourat, *At. Data Nucl. Data Tables* **129–130**, 101281 (2019).
- [34] T. Minami, M. S. Pindzola, T.-G. Lee, and D. R. Schultz, *J. Phys. B: At. Mol. Opt. Phys.* **39**, 2877 (2006).
- [35] A. Jorge, J. Suárez, C. Illescas, L. F. Errea, and L. Méndez, *Phys. Rev. A* **94**, 032707 (2016).
- [36] S. U. Alladustov, I. B. Abdurakhmanov, A. S. Kadyrov, I. Bray, and K. Bartschat, *Phys. Rev. A* **99**, 052706 (2019).
- [37] M. Baxter and T. Kirchner, *Phys. Rev. A* **93**, 012502 (2016).
- [38] J. M. Monti, R. D. Rivarola, and P. D. Fainstein, *J. Phys. B: At. Mol. Opt. Phys.* **44**, 195206 (2011).
- [39] L. F. Errea, A. Macías, L. Méndez, and A. Riera, *J. Phys. B: At. Mol. Opt. Phys.* **33**, 1369 (2000).
- [40] N. L. Guevara, E. Teixeira, B. Hall, Y. Öhrn, E. Deumens, and J. R. Sabin, *Phys. Rev. A* **83**, 052709 (2011).
- [41] L. F. Errea, C. Illescas, A. Jorge, L. Méndez, I. Rabadán, and J. Suárez, *J. Phys.: Conf. Ser.* **576**, 012002 (2015).
- [42] M. K. Pandey, Y.-C. Lin, and Y. K. Ho, *Phys. Plasmas* **20**, 022104 (2013).
- [43] M. Purkait, A. Dhara, S. Sounda, and C. R. Mandal, *J. Phys. B: At. Mol. Opt. Phys.* **34**, 755 (2001).
- [44] P. C. Stancil, J.-P. Gu, C. C. Havener, P. S. Krstic, D. R. Schultz, M. Kimura, B. Zygelman, G. Hirsch, R. J. Buenker, and M. E. Bannister, *J. Phys. B: At. Mol. Opt. Phys.* **31**, 3647 (1998).
- [45] H. C. Tseng and C. D. Lin, *J. Phys. B: At. Mol. Opt. Phys.* **32**, 5271 (1999).
- [46] S. Sounda, A. Dhara, M. Purkait, and C. Mandal, *Eur. Phys. J. D* **38**, 257 (2006).
- [47] I. B. Abdurakhmanov, J. J. Bailey, A. S. Kadyrov, and I. Bray, *Phys. Rev. A* **97**, 032707 (2018).
- [48] I. B. Abdurakhmanov, K. Massen-Hane, S. U. Alladustov, J. J. Bailey, A. S. Kadyrov, and I. Bray, *Phys. Rev. A* **98**, 062710 (2018).
- [49] J. Faulkner, I. B. Abdurakhmanov, S. U. Alladustov, A. S. Kadyrov, and I. Bray, *Plasma Phys. Control. Fusion* **61**, 095005 (2019).
- [50] A. M. Kotian, C. T. Plowman, I. B. Abdurakhmanov, I. Bray, and A. S. Kadyrov, *Atoms* **10**, 144 (2022).
- [51] N. W. Antonio, C. T. Plowman, I. B. Abdurakhmanov, I. Bray, and A. S. Kadyrov, *J. Phys. B: At. Mol. Opt. Phys.* **54**, 175201 (2021).
- [52] N. W. Antonio, C. T. Plowman, I. B. Abdurakhmanov, I. Bray, and A. S. Kadyrov, *Phys. Rev. A* **106**, 012822 (2022).
- [53] N. W. Antonio, C. T. Plowman, I. B. Abdurakhmanov, I. Bray, and A. S. Kadyrov, *Atoms* **10**, 137 (2022).
- [54] A. M. Kotian, C. T. Plowman, I. B. Abdurakhmanov, I. Bray, and A. S. Kadyrov, *J. Phys. B: At. Mol. Opt. Phys.* **55**, 115201 (2022).
- [55] E. Clementi and C. Roetti, *At. Data Nucl. Data Tables* **14**, 177 (1974).
- [56] A. Kramida, Y. Ralchenko, J. Reader, and NIST ASD Team, NIST Atomic Spectra Database, available at <https://physics.nist.gov/asd> (National Institute of Standards and Technology, Gaithersburg, 2022), version 5.10.
- [57] I. B. Abdurakhmanov, A. S. Kadyrov, and I. Bray, *Phys. Rev. A* **94**, 022703 (2016).
- [58] C. T. Plowman, I. B. Abdurakhmanov, I. Bray, and A. S. Kadyrov, *Eur. Phys. J. D* **76**, 31 (2022).
- [59] I. J. Thompson and A. R. Barnett, *Comput. Phys. Commun.* **36**, 363 (1985).
- [60] H. Takahasi and M. Mori, *Publ. Res. Inst. Math. Sci.* **9**, 721 (1973).
- [61] I. B. Abdurakhmanov, A. S. Kadyrov, S. K. Avazbaev, and I. Bray, *J. Phys. B: At. Mol. Opt. Phys.* **49**, 115203 (2016).
- [62] D. H. Crandall, R. A. Phaneuf, and F. W. Meyer, *Phys. Rev. A* **19**, 504 (1979).
- [63] N. Toshima, *Phys. Rev. A* **59**, 1981 (1999).
- [64] I. B. Abdurakhmanov, C. Plowman, A. S. Kadyrov, I. Bray, and A. M. Mukhamedzhanov, *J. Phys. B: At. Mol. Opt. Phys.* **53**, 145201 (2020).